Characteristics of turbulent flow in a cross-flow fan and its control using tubercles

Wonhyuck Yoon
Department of Mechanical & Aerospace Engineering
Seoul National University

Abstract

Flow structures in a cross-flow fan at Re = 5400 based on the blade chord length and the tip velocity at the outer radius are investigated using large eddy simulation with an immersed boundary method. An eccentric vortex near a stabilizer, flow separation on blade suction surfaces in inflow region, and a recirculation region at the corner of inflow region are obtained from simulations. To analyze the effects of these flow structures on the fan performance, the variation of the torque coefficient of each blade along the azimuthal direction is examined. Consequently, the flow separation on the blades produces oscillatory variations of the torque coefficient along the azimuthal direction, causing degraded fan performance. Moreover, the recirculation region, which is also originated from flow separation, is shown to produce a considerable loss, and the blades nearby suffer from high torque. To control the flow separations on the blades, a biomimetic control device that imitates Humpback whale's tubercle structures are used. As a result, the separation on the blades in the inflow region and the oscillation of the torque coefficient are considerably attenuated. In addition, the recirculation region and the high peak of torque coefficient are also removed. The optimal shape is obtained by a parametric study and

response surface method, and fan efficiency was improved up to 8.45%.

Keywords: cross-flow fan, flow separation, recirculation region, torque coefficient, biomimetic flow control, tubercle

Student Number: 2016-20660

Contents

List of Figures

List of Tables

Nomenclature

Roman symbols

A_{tub}	Length of the amplitude of a tubercle
$b_i, b_{ij}, \mathbf{b}$	Coefficients of a second-order response surface and a vector form of the coefficients, respectively
c	Blade chord length
f_i	Momentum forcing
$f, \hat{f}, \mathbf{f}$	Response function, approximated response function, and a vector form of the response function, respectively
L_z	Spanwise domain length
$p(=p_s)$	Static pressure
p_v	Dynamic pressure, $p_v = \rho\left\|\vec{u}\right\|^2 / 2$
p_t	Total pressure, $p_t = p_s + p_v$
p_{avg}	Averaged pressure
P_{tub}	Length of the period of a tubercle
q	Mass source/sink
Q	Volume flow rate
Re	Reynolds number, $\mathrm{Re} = U_{tip} c / \nu$
S_{ij}	Strain rate tensor, $S_{ij} = (\partial u_i / \partial x_j + \partial u_j / \partial x_i) / 2$
t	Time
$u_i(u,v,w)$	Velocity components in a Cartesian coordinate
u_{avg}	Averaged velocity
$\left\|\vec{u}\right\|$	Velocity magnitude

U_{tip}	Blade tip velocity at the outer radius
$x_i(x,y,z)$	Components of a Cartesian coordinate

Greek symbols

δ_{ij}	Kronecker delta
η	Fan efficiency
θ	Azimuthal angle
ν	Kinematic viscosity
ν_T	Eddy viscosity
ξ_1, ξ_2	Input variables for a response surface
$\boldsymbol{\Xi}$	Matrix of input variables
ρ	Density
τ_{ij}	Subgrid-scale stress tensor, $\tau_{ij} = \overline{u_i u_j} - \bar{u}_i \bar{u}_j$
τ, τ^*	Torque, torque coefficient, respectively, $\tau^* = (\tau / \rho U_{tip}{}^2 c^3) / (L_z / c)$
ϕ	Pseudo-pressure
ω_z	Spanwise vorticity
Ω	Angular velocity

Other symbols

$(\bullet)^n$	Computational time step
$(\bullet)^*$	Intermediate step
$\overline{(\bullet)}$	Filtered quantity
$\widetilde{(\bullet)}$	Test filtered quantity
$\langle \bullet \rangle_V$	Volume averaging operation

Chapter 1
Introduction

A cross-flow fan, a type of a fan that has a unique shape and a special mechanism of inducing flow, was invented by Paul Mortier in 1892 and was adopted in mine ventilating systems. However, it had not attracted the attention of engineers until the mid-twentieth century, when Ackeret suggested using the fan to suction boundary layers. After Ackeret, Eck attempted flow visualization to investigate the flow inside a cross-flow fan for the first time and found a line vortex, which is eccentric to the axis of rotation. Eck's investigation showed that the eccentric vortex characterizes the flow inside a cross-flow fan, and it has been a remarkable study, which accelerated engineers' studies on the cross-flow fan (Eck, 1973; Porter and Markland, 1970; Tuckey, 1983; Yamafuji, 1975).

The visualization of Eck showed that the eccentric vortex is formed in the cross-flow fan and it induces through flow. At that time, the cross-flow fan used by Eck did not have a casing, unlike a cross-flow fan currently used. Instead, he stabilized the vortex with an internal structure, which breaks the geometric symmetry of the fan. Then, a vortex made by the rotation of the fan was fixed to one side, which is called an eccentric vortex, and the vortex induced the through flow. After the fan of Eck was introduced, it was adopted for ventilating system. However, the manufacturing procedure was too complicated and expensive so that its usage gradually decrease. Then, Eck found out that a casing with appropriate geometry can stabilize the formed vortex. Since the casing, which is called a stabilizer, can be simply made, cross-flow fans have been widely used in ventilating systems, air-conditioners, and air-curtains (Govardhan and Sampat, 2005; Toffolo, Lazzaretto and Margegani, 2004).

After Eck's study, numerous researchers have sought for an analytic model that explains the flow structure inside a cross-flow fan. Their attempts are mainly based on potential theory, but the models did not predict the flow accurately or they included too many empirical relations (Coester, 1959; Ilberg and Sadeh, 1965; Tuckey, 1983). Therefore,

experimental and numerical investigations were necessary. In addition, as cross-flow fans have been applied a lot, lots of researches have aimed to enhance the fan efficiency. (Murata and Nishihara, 1976; Ouyang, Tian, Li, Zheng and Du, 2012; Toffolo, Lazzaretto and Margegani, 2004)

However, experimental flow visualization, such as PIV (particle image velocimetry), have been rarely performed, and numerical study was mainly based on two-dimensional RANS (Reynolds-averaged Navier-Stokes) equations so that both experimental and numerical studies were not sufficient to predict flow characteristics inside cross-flow fans. Furthermore, studies to improve the fan performances were not entirely based on understandings of flow characteristics, but focused on huge parametric studies on fan and casing geometries to obtain extensive databases.

Therefore, to predict characteristics of turbulent flow in cross-flow fans, LES (large eddy simulations) are used in this study. Then, based on the obtained flow characteristics, a flow control device is used to attenuate losses in the flow. More precisely, a biomimetic device, which is inspired by Humpback whale's tubercle structure, is used, and the geometry of the device is optimized using a parametric study and an optimization method.

Chapter 2
Numerical details

2.1. Governing equations and numerical methods

The governing equations are the spatially filtered, three-dimensional, unsteady, and incompressible continuity equation (2.1) and Navier-Stokes equations (2.2) in a Cartesian coordinate system.

$$\frac{\partial \overline{u}_i}{\partial x_i} - q = 0 \tag{2.1}$$

$$\frac{\partial \overline{u}_i}{\partial t} + \frac{\partial (\overline{u}_i \overline{u}_j)}{\partial x_j} = -\frac{\partial \overline{p}}{\partial x_i} + \frac{1}{\mathrm{Re}} \frac{\partial^2 \overline{u}_i}{\partial x_j \partial x_j} - \frac{\partial \tau_{ij}}{\partial x_j} + f_i \tag{2.2}$$

u_i and p represent the non-dimensional velocity components u, v, w and pressure, respectively. Since the simulations are conducted on staggered grid systems, each velocity component are defined at the cell faces, and pressure is defined at the cell center. An immersed boundary method (IBM) (Kim, Kim and Choi, 2001) is used to satisfy the no-slip boundary conditions, and q and f_i are mass source/sink and momentum forcing, respectively, which are assigned to the inner and boundary points of solid bodies.

LES are performed to predict turbulent flows. A spatial box filter was applied to the governing equations, which is denoted by the bar symbol $\overline{(\bullet)}$, and the corresponding subgrid-scale (SGS) stress tensor is denoted by $\tau_{ij} (= \overline{u_i u_j} - \overline{u}_i \overline{u}_j)$. The SGS stress tensor is modelled with the Smagorinsky eddy viscosity model (2.3), and the eddy viscosity ν_T was obtained by the Vreman model (2.4) and a dynamic global model (2.5) based on the Germano identity and the least square method suggested by Lilly. Here, the tilde symbol $\tilde{(\bullet)}$ and the bracket operator $\langle \bullet \rangle_V$ represent a test filter and the volume averaging operation, respectively (Germano and Sampat, 2005; Lee and Choi, 2012; Lilly, 1992; Park, Lee, Lee and Choi, 2006)

$$\tau_{ij} - \frac{1}{3}\tau_{kk}\delta_{ij} = -2\nu_T \bar{S}_{ij},$$
$$\bar{S}_{ij} = \frac{1}{2}\left(\frac{\partial \bar{u}_i}{\partial x_j} + \frac{\partial \bar{u}_j}{\partial x_i}\right) \tag{2.3}$$

$$\nu_T = C_\nu \sqrt{\frac{II_\beta}{\bar{\alpha}_{ij}\bar{\alpha}_{ij}}},$$
$$\bar{\alpha}_{ij} = \frac{\partial \bar{u}_j}{\partial x_i}, \tag{2.4}$$
$$II_{\bar{\beta}} = \bar{\beta}_{11}\bar{\beta}_{22} - \bar{\beta}_{12}{}^2 + \bar{\beta}_{11}\bar{\beta}_{33} - \bar{\beta}_{13}{}^2 + \bar{\beta}_{22}\bar{\beta}_{33} - \bar{\beta}_{23}{}^2,$$
$$\bar{\beta}_{ij} = \sum_{m=1}^{3} \bar{\Delta}_m{}^2 \bar{\alpha}_{mi}\bar{\alpha}_{mj}$$

$$C_\nu = -\frac{1}{2}\frac{\langle L_{ij}M_{ij}\rangle_V}{\langle M_{ij}M_{ij}\rangle_V},$$
$$L_{ij} = \bar{u}_i\bar{u}_j - \tilde{\bar{u}}_i\tilde{\bar{u}}_j, \tag{2.5}$$
$$M_{ij} = \sqrt{\frac{II_{\tilde{\bar{\beta}}}}{\tilde{\bar{\alpha}}_{ij}\tilde{\bar{\alpha}}_{ij}}}\tilde{\bar{S}}_{ij} - \sqrt{\frac{II_{\bar{\beta}}}{\bar{\alpha}_{ij}\bar{\alpha}_{ij}}}\bar{S}_{ij}$$

In order to solve the governing equations (2.1) and (2.2), a second-order fully implicit fractional step method with Crank-Nicolson method is used for time integration. For the non-linear convection term, a second-order linearization method $\bar{u}_i^{n+1}\bar{u}_j^{n+1} = \bar{u}_i^{n}\bar{u}_j^{n+1} + \bar{u}_i^{n+1}\bar{u}_j^{n} - \bar{u}_i^{n}\bar{u}_j^{n} + O(\Delta t^2)$ is applied (Kim, Baek and Sung, 2002):

$$\frac{\bar{u}_i^{*} - \bar{u}_i^{n}}{\Delta t} = -\frac{\partial \bar{p}^n}{\partial x_i} + \frac{1}{2\,\mathrm{Re}}\left[\frac{\partial^2 \bar{u}_i^{*}}{\partial x_j \partial x_j} + \frac{\partial^2 \bar{u}_i^{n}}{\partial x_j \partial x_j}\right] - \frac{1}{2}\left[\frac{\partial(\bar{u}_i^{*}\bar{u}_j^{n})}{\partial x_j} + \frac{\partial(\bar{u}_i^{n}\bar{u}_j^{*})}{\partial x_j}\right]$$
$$+\frac{1}{2}\left[\frac{\partial}{\partial x_j}\left(\nu_T \frac{\partial \bar{u}_i^{*}}{\partial x_j}\right) + \frac{\partial}{\partial x_j}\left(\nu_T \frac{\partial \bar{u}_i^{n}}{\partial x_j}\right)\right] + \frac{1}{2}\left[\frac{\partial}{\partial x_j}\left(\nu_T \frac{\partial \bar{u}_j^{*}}{\partial x_i}\right) + \frac{\partial}{\partial x_j}\left(\nu_T \frac{\partial \bar{u}_j^{n}}{\partial x_i}\right)\right] + f_i^{n+1} \tag{2.6}$$

$$\frac{\partial^2 \phi^n}{\partial x_j \partial x_j} = \frac{1}{\Delta t}\left(\frac{\partial \bar{u}_j^{*}}{\partial x_j} - q\right) \tag{2.7}$$

$$\bar{u}_i^{n+1} = \bar{u}_i^{*} - \Delta t \frac{\partial \phi^n}{\partial x_i} \tag{2.8}$$

$$p^{n+1} = p^n + \phi^n - \frac{\Delta t}{2\,\mathrm{Re}} \frac{\partial^2 \phi}{\partial x_j \partial x_j} \tag{2.9}$$

where $\bar{u}_i^*$ and ϕ are the intermediate velocity components and the pseudo-pressure, respectively, for the fractional step method. Also, the second-order central difference method is used for all spatial derivatives except for the derivatives at the boundary where one-side difference method is used.

During the first few revolutions of a cross-flow fan, time step size is determined so that the Courant-Friedrichs-Lewy (CFL) number is less than 1.5, and then it is fixed to a constant after the flow is developed sufficiently.

2.2. Computational details and boundary conditions

Figure 2.1 shows a schematic diagram of a cross-flow fan, a reference frame, a computational domain, and boundary conditions. The cross-flow fan is composed of an impeller, a stabilizer, and a rearguide, and its configuration is obtained by 3D-scanning the air-conditioner, model name SNQ090BS6W, of LG Electronics. After the 3D-scanning procedure, blades of the impeller are reverse designed with the two-arcs blade design method.

The impeller has 37 blades, and its outer diameter is 93.4 mm, which is 7.2 times the chord length of a blade, c (=13.1 mm). The impeller rotates in the counterclockwise direction (the $+z$ direction) and its rotational speed is 1,250 rpm, and the corresponding blade tip velocity at the outer diameter, U_{tip}, is 6.11 m/s. All non-dimensionalization is based on the blade chord length c and the tip velocity U_{tip}, and the corresponding Reynolds number is $\mathrm{Re} = U_{tip} c / \nu = 5,400$.

A constant volume flow rate 10.5 CMM (m^3/min), which is measured from experiments, is given at the inflow region with the flat velocity profile, and the heat exchanger is not included in the simulations (see 2.3). The Neumann boundary condition and the periodic boundary condition are imposed at the outflow region and in the axial direction (z -

direction), respectively. On the remaining boundaries, the no-slip boundary conditions are assigned, so that a real-scale room is depicted through the boundary conditions. Moreover, by implementing a sponge layer at the outflow region, which uses a 1:2:1 filter (Kaltenbach and Choi, 1995; Tim, Lele and Moin, 1993), vortices convecting the downstream are dissipated, and the simulations are conducted without any issue related to divergence.

When the impeller without a flow control device (base model) is used, the size of the computational domain is $250c(x)\times150c(y)\times4c(z)$, which is $3.28(\mathrm{m})\times1.97(\mathrm{m})\times52.5(\mathrm{mm})$ in real-scale, and the number of grid points in each direction is $913(x)\times1036(y)\times51(z)$, where the total number of grid points is 48 million.

After understanding the characteristics of flow inside the cross-flow fan with the base impeller, a flow control device, Humpback whale tubercle structure, is used (see chapter 4). For the controlled case, the size of the computational domain is $250c(x)\times150c(y)\times L_z(z)$, where L_z is 0.957c, 1.67c, 2.39c, or 1.56c (for the optimal geometry, see 4.4) and the corresponding number of grid points in each direction is $913(x)\times1036(y)\times N_z(z)$, where N_z is 13, 21, 31, and 21 (see 4.2).

2.3. The inflow boundary condition

Since pressure drop due to a heat exchanger at the inflow region is not modelled in the present study, the geometry of the heat exchanger is also not included in the simulations. Instead, a constant volume flow rate is given at the inflow boundary. If the Neumann boundary condition is assigned at the boundary, a volume flow rate larger than the exact value would be induced, since the pressure drop due to the heat exchanger and its geometry are not included. Thus, a volume flow rate is assigned, and the pressure load virtually occurs at the boundary.

The volume flow rate assigned at the inflow boundary is determined experimentally. Figure 2.2 (a) shows a standard of a wind tunnel and an experimental setup for cross-flow fan experiments. The cross-flow fan is mounted at the wind tunnel entrance with a heat

exchanger, and by modulating the auxiliary fan at the wind tunnel exit, the pressure rise can be measured at various flow rates (figure 2.3). When the pressure rise is equal to zero, it means that all the pressure rise due to fan work is used to overcome the load of the heat exchanger. Thus, the simulations are performed with the volume flow rate (10.5 CMM) at which the pressure rise is zero.

2.4. Calculation of the pressure rise and the fan performance

In contrast to experiments, it is hard to measure pressure rise in numerical simulations. Thus, it is important to define the pressure rise appropriately. In the experiments, the pressure rise is obtained by measuring pressure inside a chamber (figure 2.2 (a)) (AMCA Int.), and it is assumed that the flow inside the chamber has reached an equilibrium state. Therefore, in the simulations, the pressure rise should be averaged over some plane or volume rather than measuring at a point. The simplest way to take an average is the area averaging. However, the velocity and pressure field before and after taking the area averaging do not satisfy the momentum conservation, in general. Hence, the mixed-out averaging is used in the present study.

The mixed-out averaging is an averaging method which satisfies the mass and momentum conservation (Greitzer, Tan and Graf, 2007). Let us assume a quasi-one-dimensional flow, and the velocity and pressure distribution are $u(y)$ and $p(y)$, respectively. Then, an averaging method is a procedure that finds a representative velocity and pressure, u_{avg} and p_{avg} (figure 2.4), and it is natural to make velocity and pressure satisfy the mass and momentum conservation. The mixed-out averaging is the way that assures the conservation laws (equation (2.10) and (2.11)).

$$\int_A \rho(\vec{u}\bullet\hat{n})dA = 0 \tag{2.10}$$

$$\int_A \rho\vec{u}(\vec{u}\bullet\hat{n})dA = -\int_A p\hat{n}dA \tag{2.11}$$

From the above equations, u_{avg} and p_{avg} can be calculated through equations (2.12) and (2.13)

$$u_{avg} = \frac{1}{H}\int_1 u dy \tag{2.12}$$

$$p_{avg} = \frac{1}{H}\int_1 (\rho u^2 + p) dy - \rho {u_{avg}}^2 \tag{2.13}$$

Moreover, the standard with a free inlet, which is depicted in figure 2.2 (a), is used for the experiments, but the simulation setting corresponds to the standard with a free outlet, which is shown in figure 2.2 (b). Consequently, $p_{s,inlet} = 0$ and $p_{v,inlet} = 0$ for the experiments, but $p_{s,outlet} = 0$ only for the simulations. Thus, the total pressure rise in the simulations can be calculated by the equation (2.14), where the abbreviation avg. means mixed-out averaging.

$$\begin{aligned} \Delta p_{t,avg} &= (p_{s,avg} + p_{v,avg})_{outlet} - (p_{s,avg} + p_{v,avg})_{inlet} \\ &= p_{v,avg,outlet} - (p_{s,avg} + p_{v,avg})_{inlet} \\ &= \frac{1}{2}\rho({u_{avg,outlet}}^2 - {u_{avg,inlet}}^2) - p_{s,avg,inlet} \end{aligned} \tag{2.14}$$

Finally, the fan efficiency is used to represent the fan performance in this study, which is defined by the ratio of the energy output to the energy input (equation 2.15). More precisely, the denominator of the equation (2.15) is the mechanical power input required to rotate an impeller with an angular velocity Ω, and the numerator is the aerodynamic power obtained by the fluid with a volume flow rate Q.

$$\eta = \frac{\Delta p_t Q}{\tau \Omega} \tag{2.15}$$

2.5. Measurement of the variation of the torque coefficient

To investigate the flow characteristics inside a cross-flow fan and their effects on the fan performance quantitatively, the variation of the torque coefficient of each blade along the azimuthal direction is measured, where the torque coefficient is defined as equation (2.16) (see 3.2).

$$\tau^* = \frac{\tau}{\rho U_{tip}{}^2 c^3} \Big/ \frac{L_z}{c} \tag{2.16}$$

The position of a blade is traced with the angle between the geometric center of the blade and the x-axis, and the angle is set to a positive value in the counterclockwise direction. For the torque coefficient, clockwise direction is recorded as a positive value, which is the direction of the torque a fan undergoes when doing positive work (see figure 3.2 in 3.2). After N revolutions, N graphs of the variation of the torque coefficient is obtained, and one variation of the torque coefficient is attained by averaging over the number of blades (37) and the number of revolutions (N) (figure 2.5).

(a)

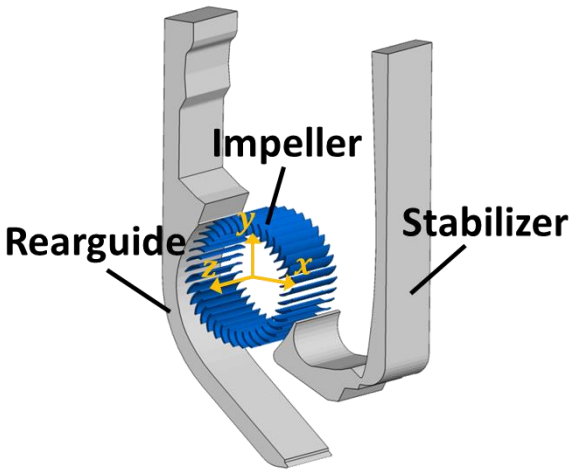

(b)

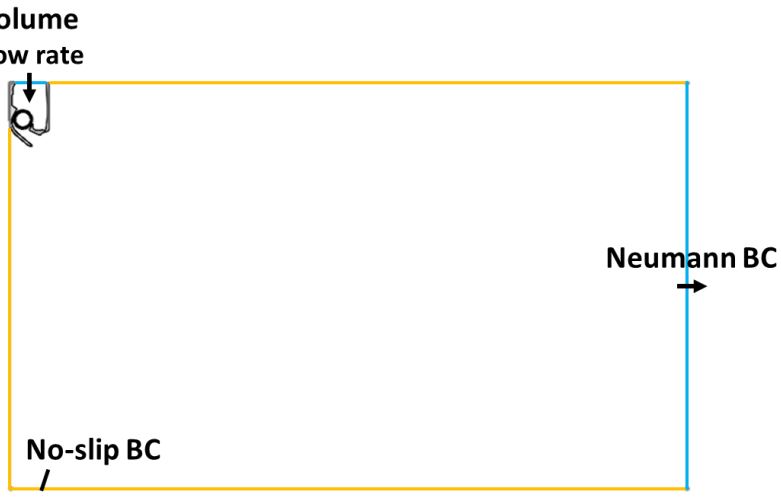

Figure 2.1 (a) Schematic diagram of a cross-flow fan; (b) computational domain and boundary conditions.

(a)

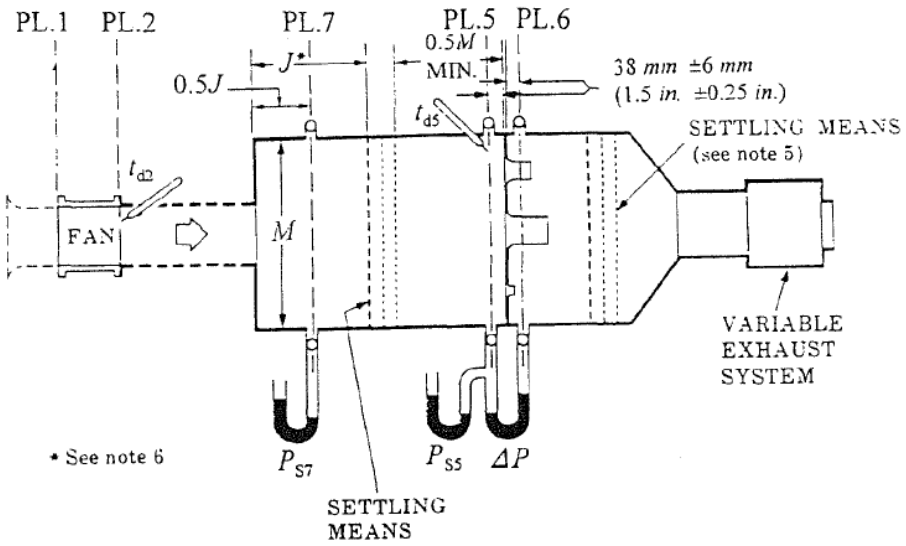

(b)

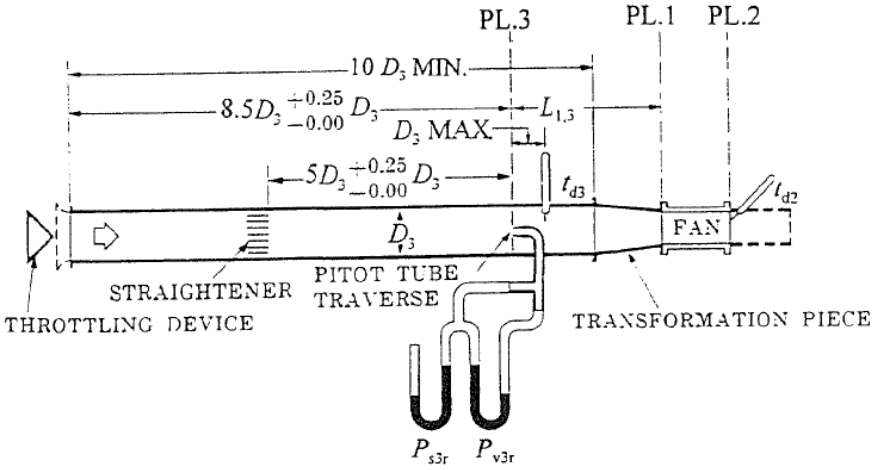

Figure 2.2 Two different standard of fan experiments: (a) outlet chamber setup-multiple nozzles in chamber; (b) inlet duct setup-pitot traverse in inlet duct (AMCA Int.).

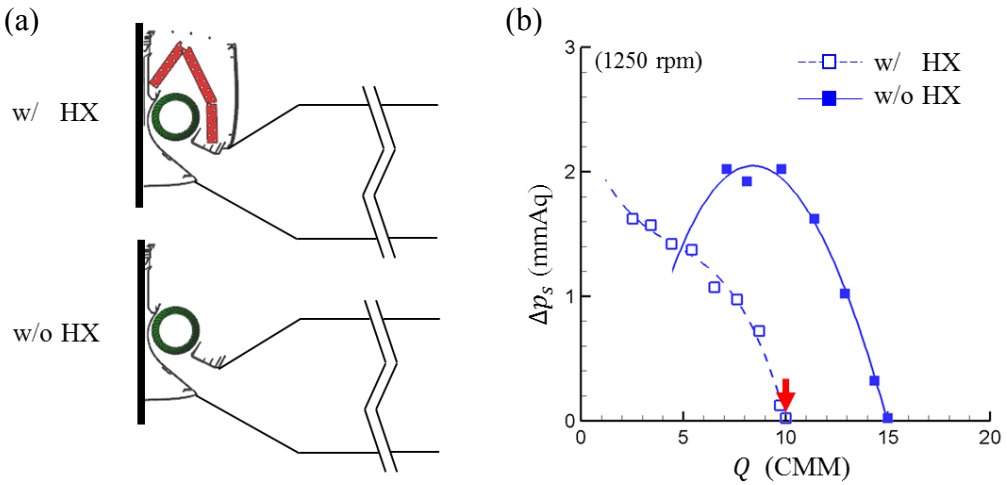

Figure 2.3 (a) Schematic diagram of an experimental setup: with a heat exchanger (top); without a heat exchanger (bottom); (b) static pressure rise vs. volume flow rate: the red arrow indicates the operating condition (10.5 CMM).

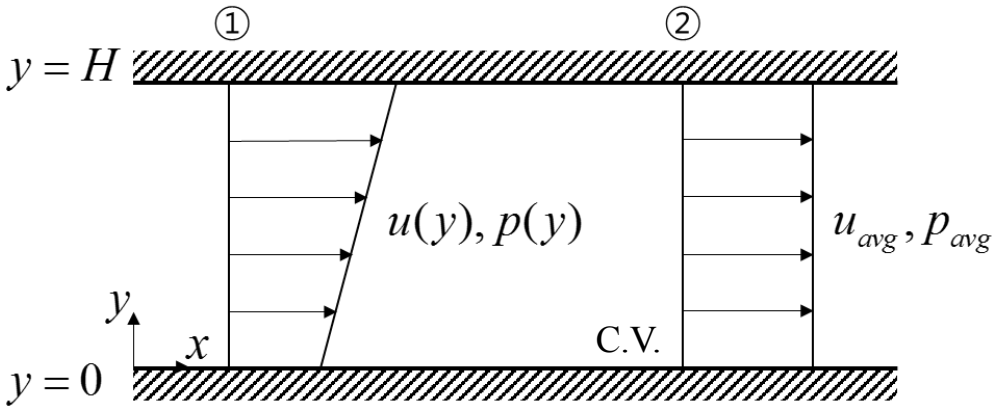

Figure 2.4 Schematic diagram of an averaging process of quasi-one-dimensional flow and a control volume.

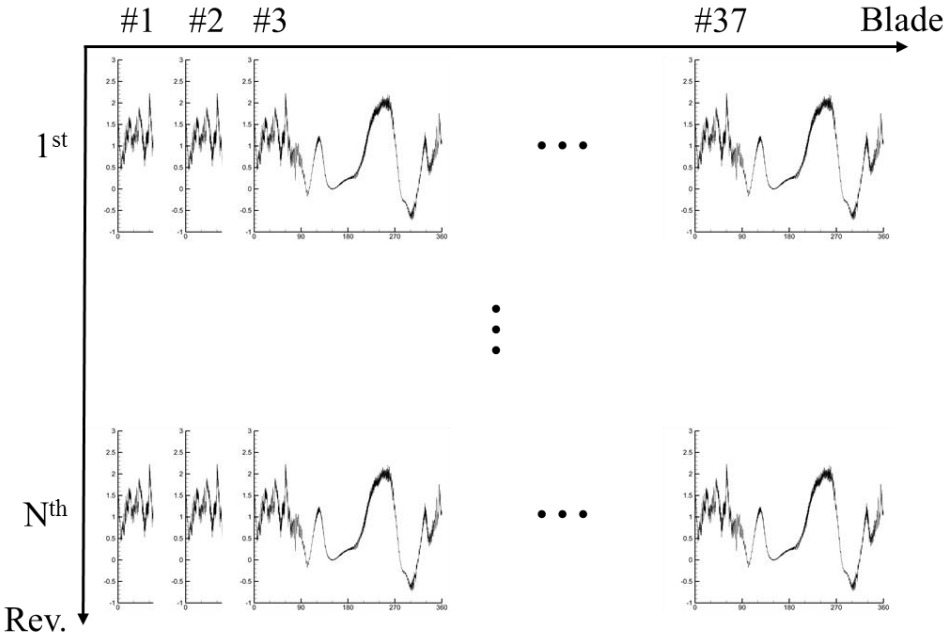

Figure 2.5 Averaging process of the variation of the torque coefficient over the blades and the revolutions.

Chapter 3
Numerical results for the base model

3.1. Overall flow characteristics

Figure 3.1 (a) shows a phase-averaged streamline inside the cross-flow fan with the base impeller, and more specific characteristics are given in figure 3.1 (b), which shows an instantaneous spanwise vorticity field ω_z. An eccentric vortex is fixed near the stabilizer, and the through flow is induced by the vortex. In the inflow region, a recirculation region at a corner near the rearguide is observed, and massive flow separations occur at the blade leading edges, which can be recognized in the vorticity contour. Moreover, the efficiency of the fan is predicted to be 0.377.

3.2. Variation of the torque coefficient

Figure 3.2 shows the variation of the averaged torque coefficient of a blade along the azimuthal direction, which is traced to examine the flow characteristics and their effects on the fan performance: The fan efficiency, which is the most representative quantity for the fan performance, is defined as the ratio of the energy output ($\Delta p_t Q$) to the energy input ($\tau\Omega$). In other words, it is the rate at which the input torque is converted to the output pressure rise. Thus, if the torque is well converted to the pressure rise, the higher positive torque, the more desirable it is. Otherwise, high positive torque lowers the fan efficiency. Therefore, high positive torque does not always mean a large amount of work, but it is necessary to analyze the surrounding flow field to determine how well it is converted. In the present study, four different regime A ~ D along the azimuthal direction can be identified by comparing the flow fields and the torque variation, which is marked in figure 3.3 (a) and (b). An analysis of whether the torque aspects appearing in each regime is loss or not will be further elaborated through 3.2.1~3.2.4.

3.2.1. Regime A (Inflow region)

A phase-averaged velocity magnitude contour and streamlines of regime A are shown in figure 3.4 (a). Because a fan is a device that does work on fluid, it must receive reacting torque, and regime A is the region where blades work sufficiently and get high torque. In figure 3.4 (a), it is observed that fluid passes through regime A accelerates and deflects its direction significantly, which implies a large momentum change, and such momentum change is appearing as high torque.

However, massive separations occur on the blade leading edges in this regime, and it can be inferred that the vortex shedding due to the separations may cause some losses, such as mixing loss (Hager, 2010). Thus, it is important to recognize the occurrence of the vortex shedding. In the present study, it seems that the vortex shedding is indicated by highly oscillatory change and 20° -interval peaks observed in the torque variation graph (figure 3.4 (b)). Although no direct evidence has yet been found on the relationship between the two phenomena, it is clear that both are repetitive phenomena because the vortex shedding and the 20°-interval peaks remain in the phase-averaged vorticity field (figure 3.4 (c)) and the averaged torque graph (figure 3.4 (b)), respectively. Thus, some correlations may exist between them. Moreover, it is indirectly confirmed from the result of applying a flow control device (see 4.4).

3.2.2. Regime B (Near the rearguide)

In regime B, a high peak of the torque coefficient is observed, and it is highly related to the recirculation region in this regime. In the previous research (Ouyang, Tian, Li, Zheng and Du, 2012), it is also noted that a torque peak in the variation of the torque coefficient appears when a recirculation region exists, but no detailed explanation has been provided. In the present study, it is suggested that separations on blades in regime B (different from the separations in regime A) are the main cause of this phenomena.

Figure 3.5 (a) shows phase-averaged streamlines, which are observed in a reference frame rotating with the impeller, and a phase-averaged pressure contour. It is shown that

the blades in this regime have high angle of attacks, which lead to separations on the blades, and separated flows block passages between the blades and prevent the inflow from flowing along the impeller. More specifically, it can be observed that the flow along the impeller in regime B has positive velocity components in the radial direction (figure 3.5 (c): velocity vector field observed in the fixed reference frame). Therefore, some of the flow returns to the right to create the recirculation region, and some collides with the rearguide so that a stagnation point flow is formed. As a result, a high pressure region is generated (figure 3.5 (c)), and the high pressure is applied to the pressure side of the blade, which is getting close to this region, resulting in a large positive torque.

In conclusion, the large torque received in this regime is not the torque that the blade receives as it works on the fluid. Instead, it is the torque due to the surrounding flow structure, which cannot be converted to the energy of the fluid. Therefore, the high peak of the torque that appears in this regime causes the degradation of the fan efficiency.

3.2.3. Regime C (Outflow region)

Figure 3.6 (a) shows a phase-averaged velocity magnitude contour and streamlines. Regime C is similar to regime A at which the blades work to the fluid appropriately, and it appears as high torque coefficient.

3.2.4. Regime D (Near the stabilizer and the eccentric vortex)

In regime D, negative torque, which implies negative work, is observed. Figure 3.7 (a) shows a phase-averaged pressure contour around the eccentric vortex. Because pressure decreases toward the center of the vortex, a pressure difference occurs between two sides of a blade, which approaches the vortex as rotating counterclockwise, thus the blade receives negative torque (clockwise direction torque). In other words, not the blade works on the fluid, but rather the energy of the fluid is transferred to the blade, in this regime. Therefore, it seems that the negative torque reduces the total torque, but the loss of the energy of fluid occurs, in reality.

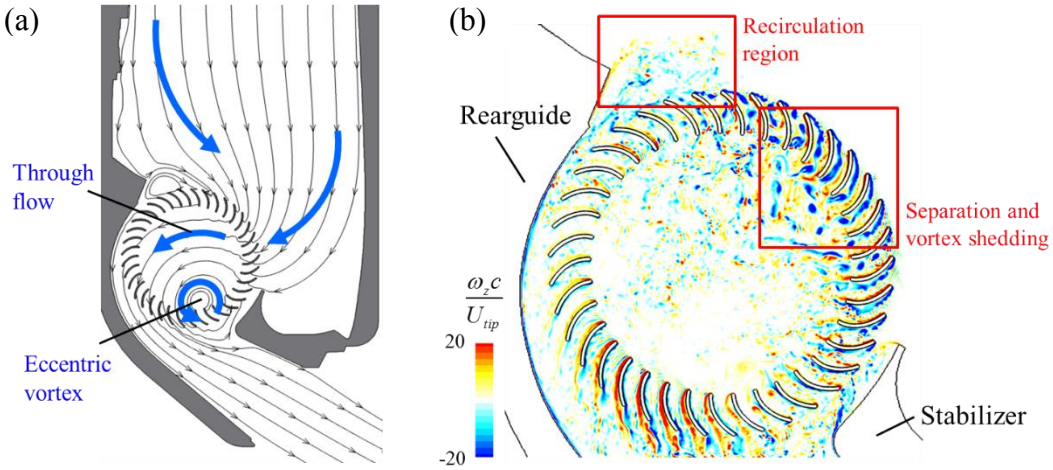

Figure 3.1 (a) Overall flow characteristics inside a cross-flow fan (phase-averaged streamline); (b) specific features of the flow (instantaneous spanwise vorticity contour): leading edge separations and a recirculation region.

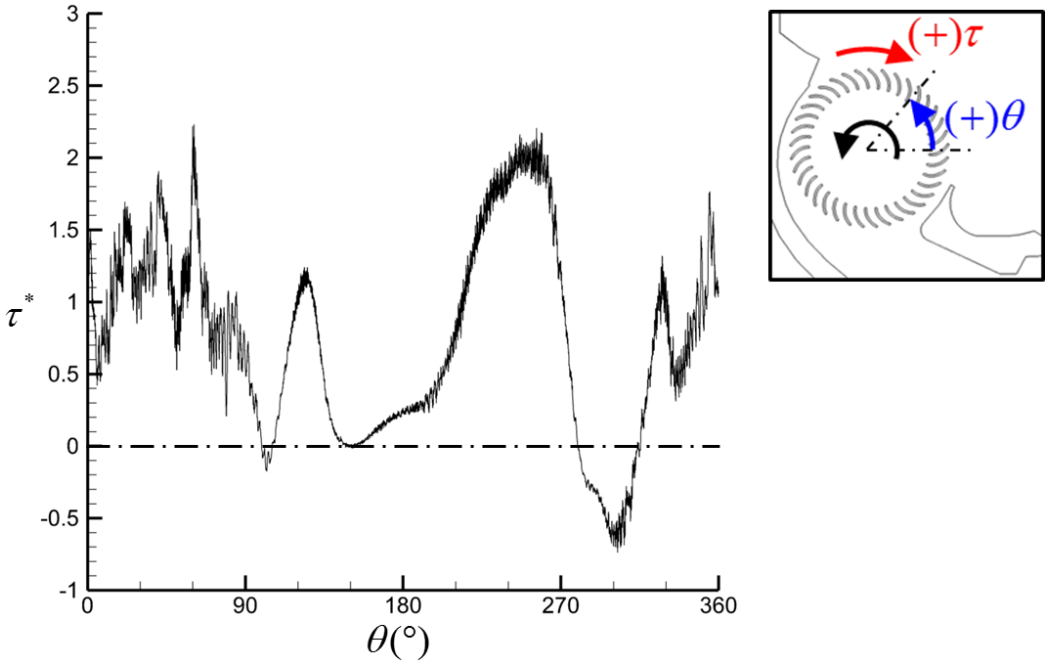

Figure 3.2 Variation of the torque coefficient along the azimuthal direction acting on a base blade.

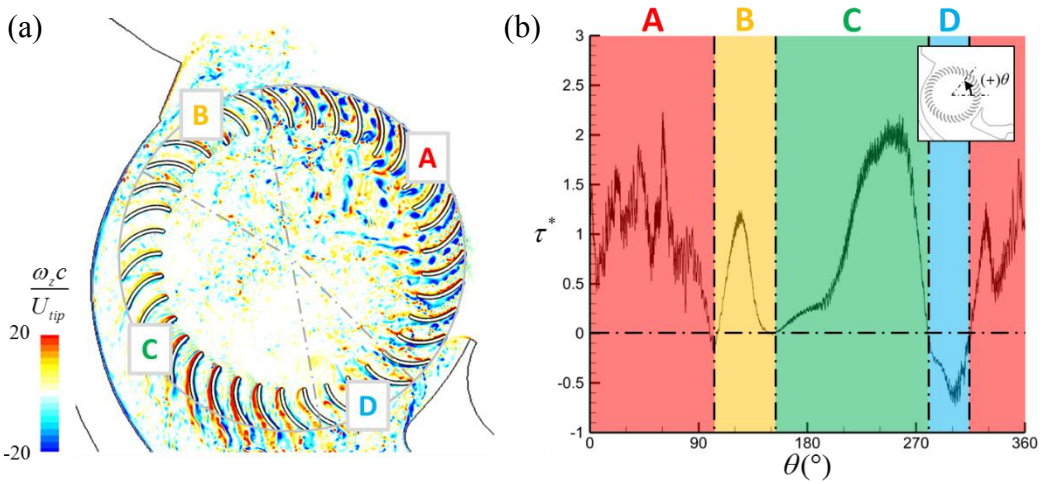

Figure 3.3 Four different regimes in the (a) flow field (instantaneous spanwise vorticity contour); (b) variation of the torque coefficient.

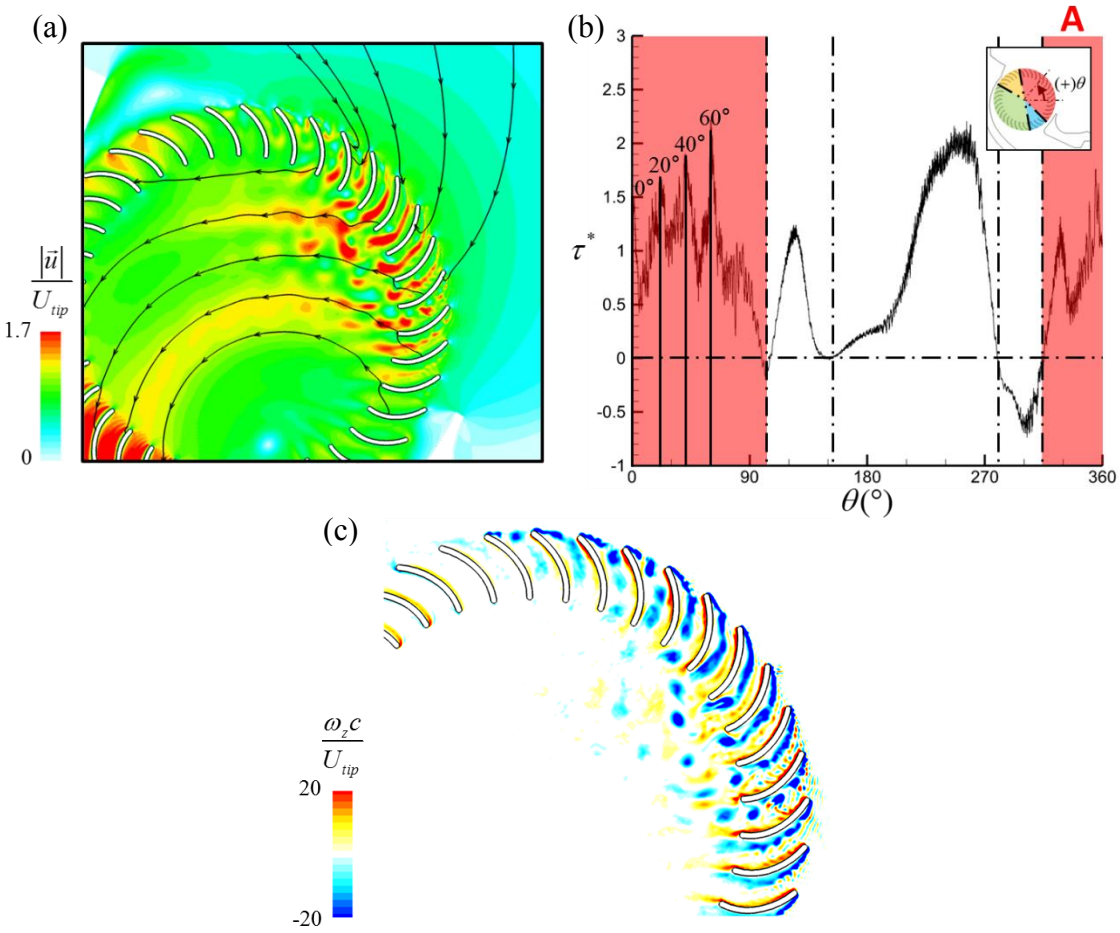

Figure 3.4 Regime A: (a) phase-averaged velocity magnitude contour and streamlines; (b) variation of the torque coefficient with 20°-interval peaks; (c) phase-averaged spanwise vorticity contour.

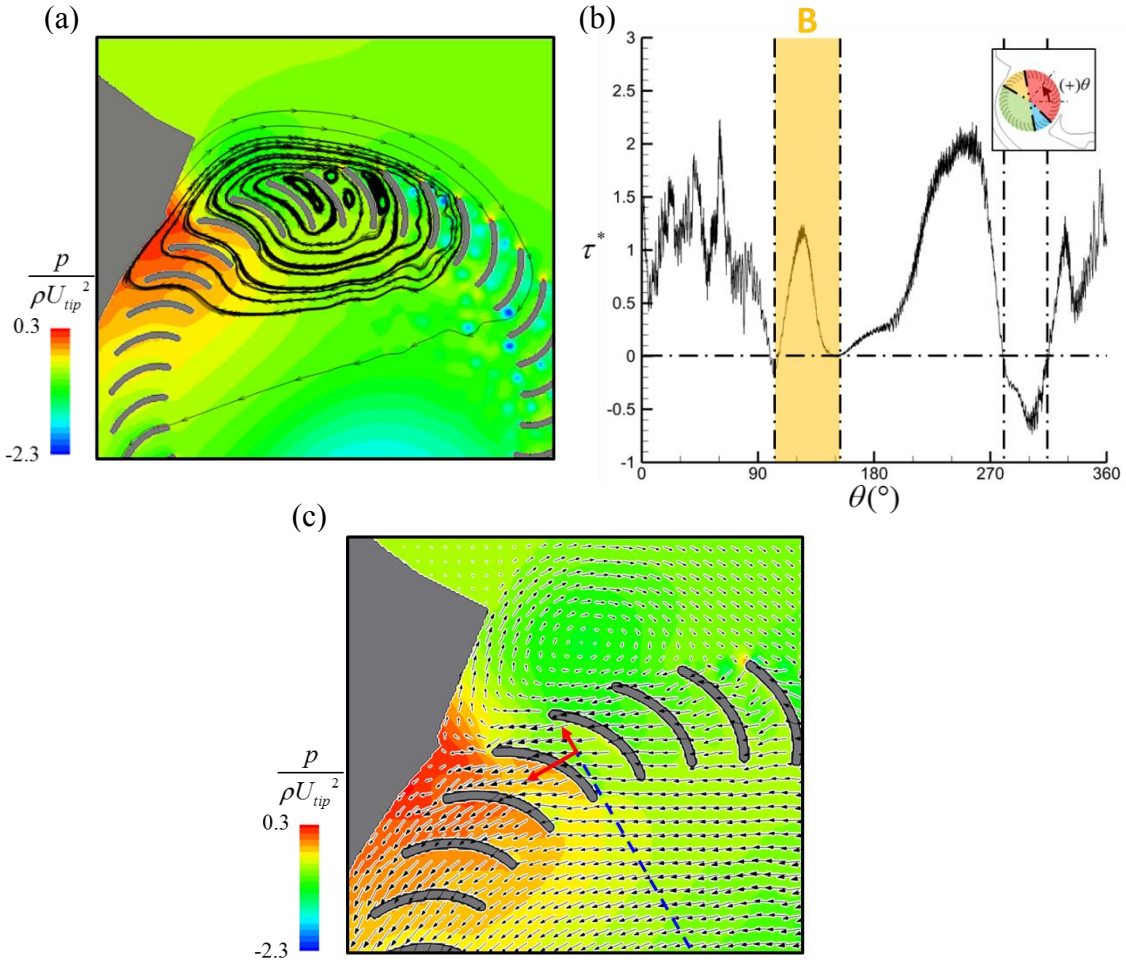

Figure 3.5 Regime B: (a) phase-averaged pressure contour and streamlines in the frame rotating with the impeller; (b) variation of the torque coefficient; (c) phase-averaged pressure contour and velocity vector field in the fixed frame.

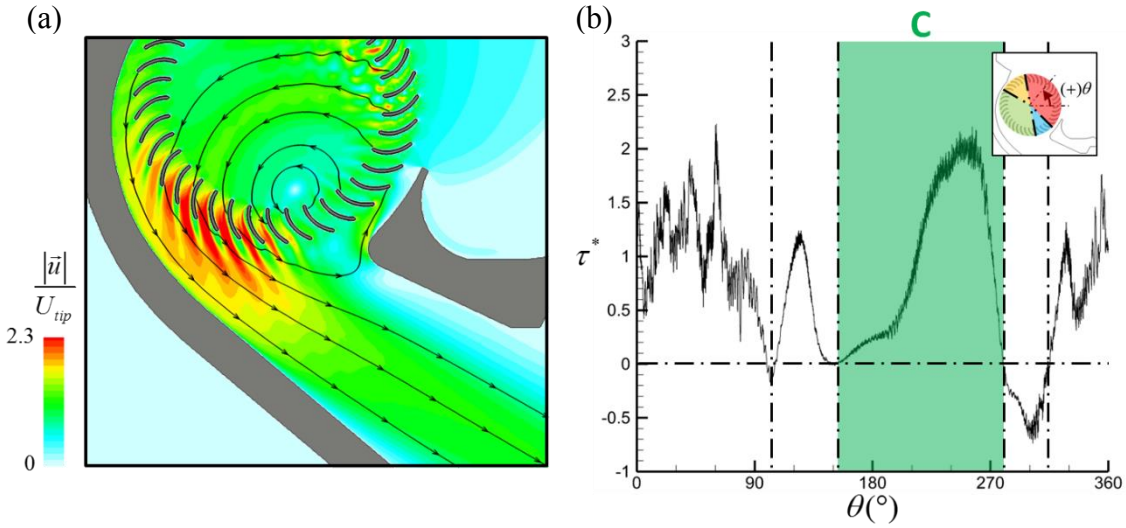

Figure 3.6 Regime C: (a) phase-averaged velocity magnitude contour and streamlines; (b) variation of the torque coefficient.

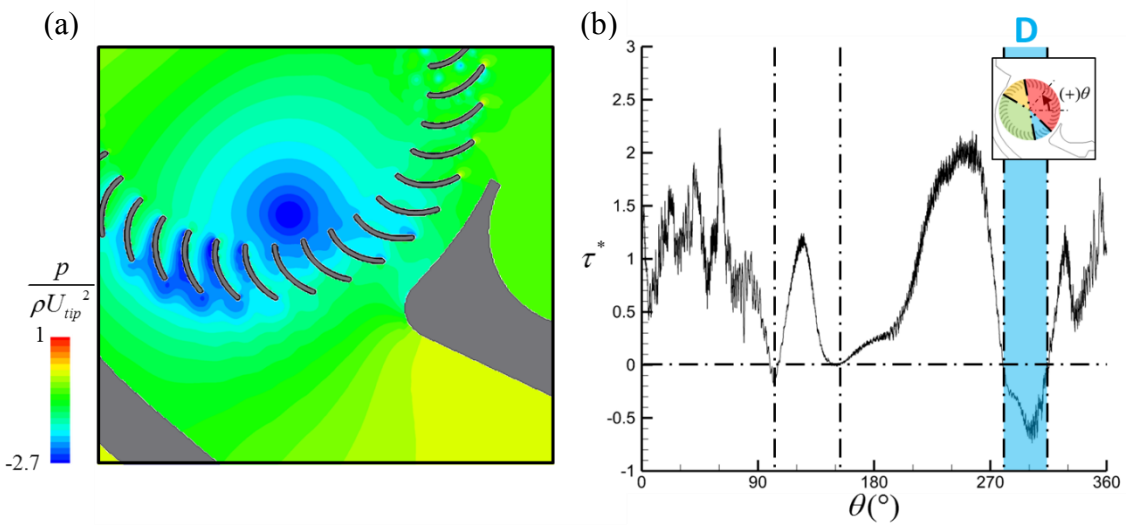

Figure 3.7 Regime D: (a) phase-averaged pressure contour; (b) variation of the torque coefficient.

Chapter 4
Flow control using tubercles

4.1. Losses in the flow

In the chapter 3, it is shown that two major losses in the flow exist. Firstly, the massive separations on the blades in regime A generate mixing loss, and secondly, the high peak of the torque in regime B degrades the fan efficiency. Moreover, the high peak of the torque is also originated from flow separation. Thus, we may introduce a flow control device that is effective for delaying separation.

4.2. Flow control method

In the present study, a biomimetic flow control device, Humpback whale's tubercle structure, is used. Humpback whale is famous for its acrobatic movement using its pectoral flippers, even though it is one of the largest whale species (Choi, Park, Sagong and Lee, 2012). Several researches have been conducted about Humpback whale's flipper, which has an array of bumps, called tubercles, on its leading edge (figure 4.1 (a)), and it has been showed that the tubercles are effective in delaying leading edge separation (Fish, Weber, Murray and Howle, 2011; Miklosovic, Murray, Howle and Fish, 2004; Van Nierop, Alben and Brenner, 2008). Therefore, an impeller with tubercles, which are modelled by a sinusoidal protrusion, is adopted (figure 4.1 (b)), then flow characteristics, the variation of the torque coefficient, and the fan efficiency are examined. Two variables P_{tub} and A_{tub} are used to design the sinusoidal protrusion, which are the period and the amplitude of the structure, respectively. For the controlled case, P_{tub} is selected as the spanwise (z -direction) size of the domain L_z ,so that the periodic boundary condition in the direction is available. In addition, the size of the grid in the spanwise direction is remained the same as that of the base model case (see 2.2).

4.3. Optimization of control device

4.3.1. Design of experiment

To optimize the geometry of the tubercle, a parametric study is conducted on two variables P_{tub} and A_{tub}. Three different values (0.957c, 1.67c, and 2.39c) are taken for the period, while four different values (0.019c, 0.038c, 0.057c, and 0.076c) are taken for the amplitude (figure 4.2). After twelve simulations are performed, a second-order response surface is obtained, and the optimal design of the geometry is found.

4.3.2. Response surface method

Using the results of the parametric study, a second-order response surface of the form as shown in equation (4.1) is obtained, where ξ_1 and ξ_2 are input variables, and $\hat{f}$ is an approximated value of a response function f. In the present study, ξ_1, ξ_2, and f corresponds to P_{tub}, A_{tub}, and the fan efficiency η, respectively.

$$\hat{f} = b_0 + b_1\xi_1 + b_2\xi_2 + b_{11}\xi_1^2 + b_{22}\xi_2^2 + b_{12}\xi_1\xi_2 \tag{4.1}$$

If k and l different values are taken for ξ_1 and ξ_2, respectively, a matrix $\mathbf{\Xi}$ is defined as a $kl \times 6$ matrix whose the first column is filled with 1, and the second columns to the sixth column have kl different combinations of $\xi_1, \xi_2, \xi_1^2, \xi_2^2$ and $\xi_1\xi_2$ (equation (4.2)). In addition, a vector $\mathbf{f}$ is a $kl \times 1$ column vector whose entries are the measured responses in the experiments, and a vector $\mathbf{b}$ is a 6×1 column vector whose entries are b_0 to b_{12} of equation (4.1) (equation (4.3) and (4.4)).

$$\mathbf{\Xi} = \begin{bmatrix} | & | & | & | & | & | \\ 1 & \xi_1 & \xi_2 & \xi_1^2 & \xi_2^2 & \xi_1\xi_2 \\ | & | & | & | & | & | \end{bmatrix} \tag{4.2}$$

$$\mathbf{f}^{\mathrm{T}} = \begin{bmatrix} — & f & — \end{bmatrix} \tag{4.3}$$

$$\mathbf{b}^{\mathrm{T}} = \begin{bmatrix} b_0 & b_1 & b_2 & b_{11} & b_{22} & b_{12} \end{bmatrix} \tag{4.4}$$

With the least square method, which minimizes the sum of squared residuals, the coefficients of the response surface $\hat{f}$ can be obtained by equation (4.5). (Myers and Montgomery, 1970)

$$\mathbf{b} = \left(\Xi^{\mathrm{T}}\Xi\right)^{-1}\Xi^{\mathrm{T}}\mathbf{f} \tag{4.5}$$

4.4. Control result

Table 4.1 shows the efficiencies of various cross-flow fans which include the impellers with tubercles, and their percentage increment with respect to the efficiency of the base model (=0.377). Among the twelve cases, the impeller which adopted the tubercle with $(P_{tub}, A_{tub}) = (1.67c, 0.057c)$ showed the best performance.

The effects of the tubercles can be identified from the change of the variation of the torque coefficient and the flow fields. The red line in figure 4.3 shows that the oscillatory variation of the torque coefficient in regime A is considerably weaken, and besides, the

		P_{tub}		
		0.957c	1.67c	2.39c
A_{tub}	0.076c	*0.334 (-11%)*	*0.331 (-12%)*	*0.276 (-27%)*
	0.057c	**0.392 (3.8%)**	**0.398 (5.6%)**	*0.374 (-0.8%)*
	0.038c	**0.390 (3.5%)**	**0.386 (2.5%)**	**0.382 (1.2%)**
	0.019c	*0.319 (-15%)*	**0.389 (3.4%)**	*0.325 (-14%)*

Table 4.1 Results of the parametric study on the tubercle geometries: efficiency and its percentage increment with respect to the efficiency of the base model (in parentheses). A number is written in bold when the value is positive; otherwise, it is written in italic.

peak in regime B also vanishes. Then, the change of the torque variation can be explained by analyzing the change of the flow fields. Firstly, in figure 4.4, it can be observed that vortex shedding due to flow separations on the blades in regime A is noticeably diminished. Thus, this phenomenon indirectly certificates that there are some relations between the vortex shedding and oscillatory variation of the torque, which is mentioned in 3.2.1. Secondly, figure 4.5 shows the change of the flow fields in regime B. Before adopting tubercles, fluid moving along the impeller has positive velocity component in the radial direction due to separations (figure 4.4 (a) and (c)), which is noted in 3.2.2. However, after adopting tubercles, the separations are delayed (i.e. separations occur at points that have larger azimuthal angles), and fluid moving along the impeller has negative velocity component in the radial direction, Thus, the recirculation region and stagnation point is removed, and the high peak also disappears (figure 4.4 (b) and (d)).

Furthermore, the maximum efficiency point on the response surface is obtained using the conjugate gradient method. The coefficients of the response surface are $\mathbf{b}^{\mathrm{T}} = \begin{bmatrix} 0.0696 & 0.200 & 8.35 & -0.0533 & -80.0 & -0.730 \end{bmatrix}$, and the maximum efficiency point is $(P_{tub}, A_{tub}) = (1.56c, 0.045c)$, which expects the maximum efficiency 0.414. A simulation at the expected maximum efficiency point is conducted, and the calculated efficiency is 0.409, which is in good agreement with the predicted value. The percentage increment of the calculated efficiency is 8.45%. Further study on the flow characteristics at the maximum point and experimental validation should be conducted in follow up studies.

(a) (b)

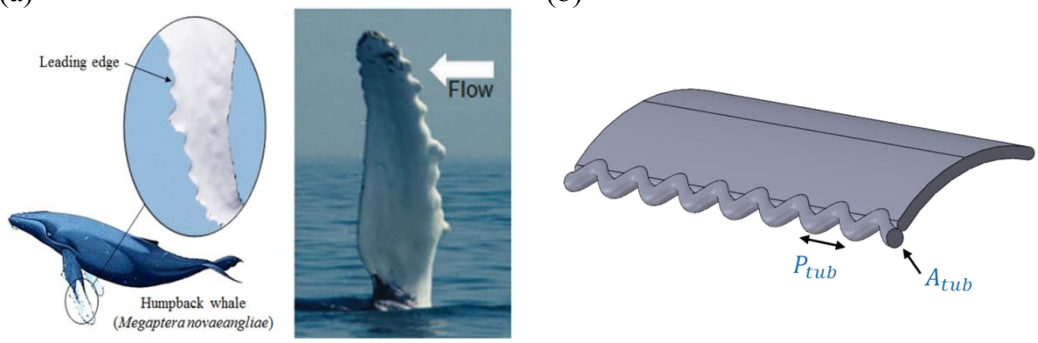

Figure 4.1 (a) Tubercle structures on Humpback whale's flipper (Choi, Park, Sagong and Lee, 2012); (b) sinusoidal protrusions, which is a flow control device mimicking tubercles, and their geometric parameters.

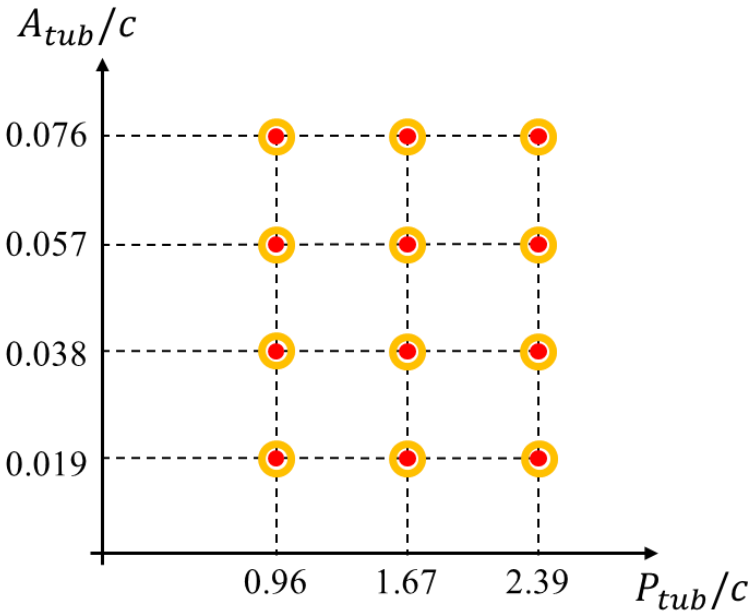

Figure 4.2 Design of experiment for a parametric study on tubercle geometry.

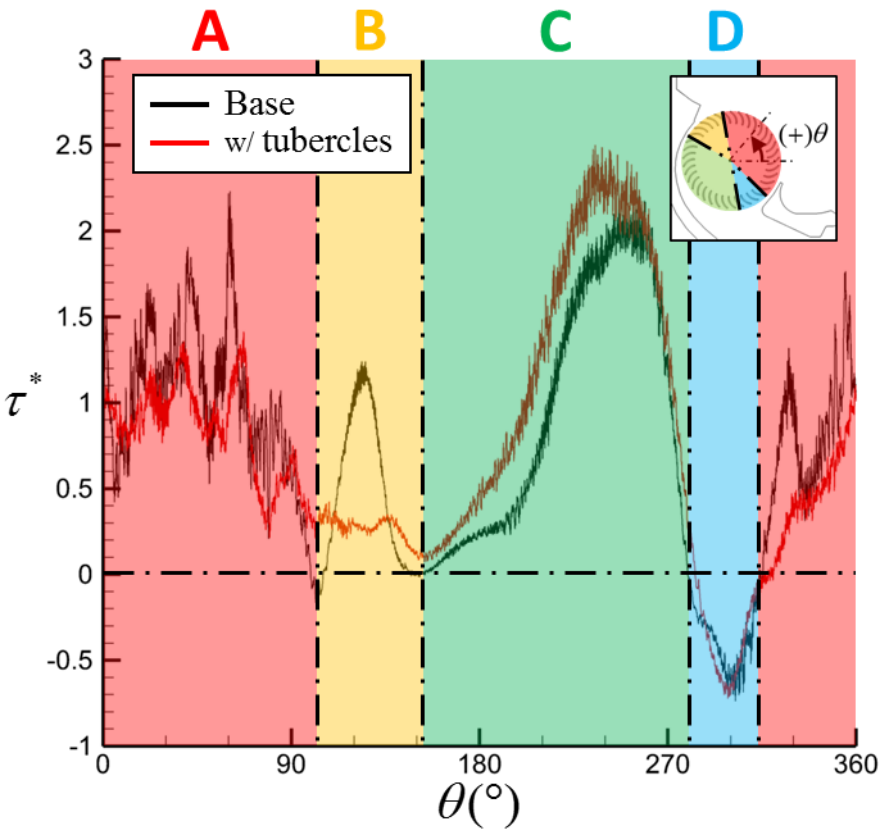

Figure 4.3 Variation of the torque coefficient along the azimuthal direction using the impeller with and without tubercles, where $(P_{tub}, A_{tub}) = (1.67c, 0.057c)$.

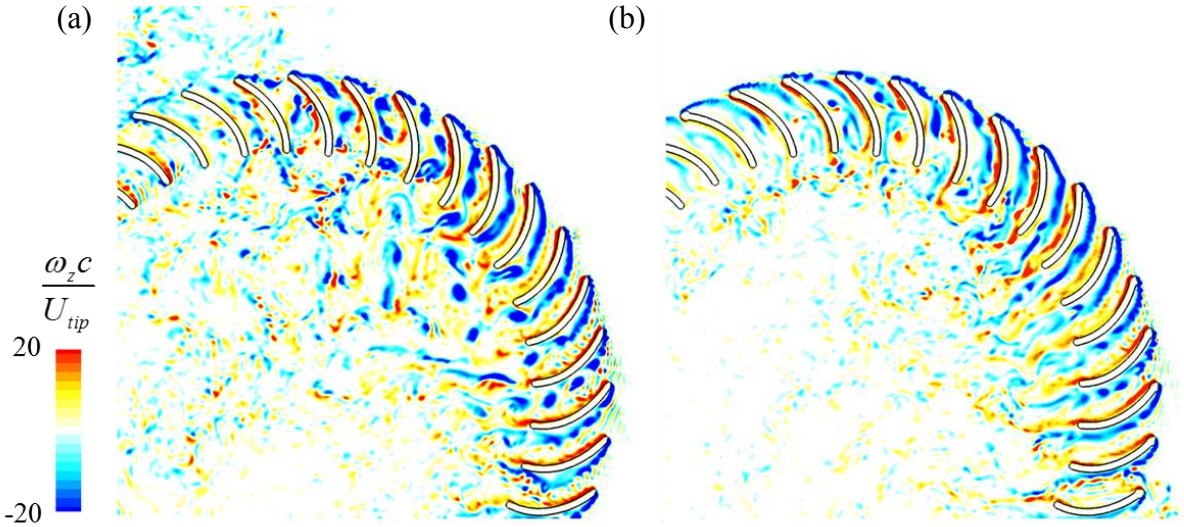

Figure 4.4 Instantaneous spanwise vorticity contour using the impeller (a) with and (b) without tubercles, where $(P_{tub}, A_{tub}) = (1.67c, 0.057c)$.

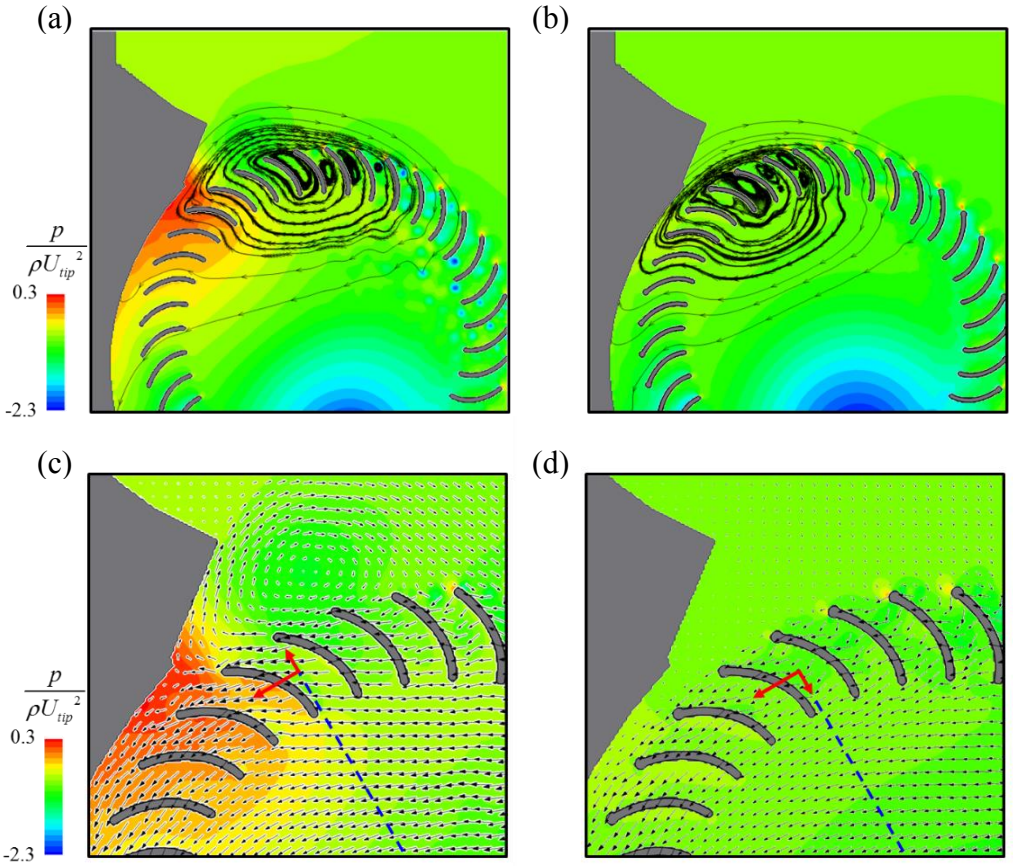

Figure 4.5 Phase-averaged pressure contour and streamlines using the impeller (a) with and (b) without tubercles; phase-averaged pressure contour and velocity vector field using the impeller (c) with and (d) without tubercles, where $(P_{tub}, A_{tub}) = (1.67c, 0.057c)$.

Conclusions

In the present study, flow characteristics inside a cross-flow fan and a biomimetic flow control method are examined. To investigate the flow characteristics quantitatively, the variation of the torque coefficient along the azimuthal direction is studied. Consequently, the torque variation showed four typical aspects, regime A with highly oscillatory variation, regime B with a peak of the torque, regime C with high torque, which indicates considerable amount of work, and regime D with negative torque. In addition, they can be identified to the features of the flow field. By analysing the flow fields, the variation of the torque coefficient and flow characteristics can be explained. Furthermore, losses in the flow among the characteristics are recognized, which are originated from separation on the blade leading edge.

After understanding the flow features and losses in the flow, a biomimetic flow control device is adopted. The device mimics Humpback whale flipper's tubercle structure, and it is applied to the blade leading edge. It is observed that the device is effective for delaying separation, which dramatically changes the streamwise vorticity field, and fan performance is improved. Moreover, the device geometry is optimized using the response surface method, and the device with the optimal geometry enhanced the fan efficiency by 8.45%. More precise analysis on the effects of the device, such as three-dimensional effect, and experimental validation should be further investigated.

References

AMCA Int. AMCA 210: laboratory methods of testing fans and ratings.

COESTER, R. 1959. Theoretische und experimentelle Untersuchungen an Querstromgebläsen. Doctoral dissertation, ETH Zurich.

CHOI, H., PARK, H., SAGONG, W. & LEE, S. I. 2012. Biomimetic flow control based on morphological features of living creatures. *Phys. Fluids* **24**, 121302.

ECK, B. 1973. *Fans–design and operation of centrifugal, axial-flow and cross fans.*

FISH, F. E., WEBER, P. W., MURRAY, M. M. & HOWLE, L. E. 2011. The tubercles on humpback whales' flippers: application of bio-inspired technology. 203-213.

GERMANO, M., PIOMELLI, U., MOIN, P. & CABOT, W. H. 1991. A dynamic subgrid-scale eddy viscosity model. *Phys. Fluids* **3**, 1760.

GOVARDHAN, M. & SAMPAT, D. L. 2005. Computational studies of flow through cross flow fans-effect of blade geometry. *J. Therm. Sci*. **14**, 220-229.

GREITZER, E. M., TAN, C. S. & GRAF, M. B. 2007. *Internal flow: concepts and applications* (Vol. 3). Cambridge University Press.

HAGER, W. H. 2010. Losses in flow. In *Wastewater Hydraulics* (pp. 17-54). Springer Berlin Heidelberg.

ILBERG, H. & SADEH, W. Z. 1965. Flow theory and performance of tangential fans. *Inst. Mech. Eng,* **180**, 481-496.

KALTENBACH, H. J. & CHOI, H. 1995. Large-eddy simulation of flow around an airfoil on a structured mesh.

KIM, J., KIM, D. & CHOI, H. 2001. An immersed-boundary finite-volume method for simulations of flow in complex geometries. *J. Comp. Phys.* **171**, 132-150.

KIM, K., BAEK, S. J. & SUNG, H. J. 2002. An implicit velocity decoupling procedure for the incompressible Navier–Stokes equations. *Int. J. Num. Methods Fluids* **38**, 125-138.

LEE, J. & CHOI, H. 2012. A dynamic global subgrid-scale model for large eddy simulation of scalar transport in complex turbulent flows. *J. Mech. Sci. Tech.* **26**, 3803-3810.

LILLY, D. K. 1992. A proposed modification of the Germano subgrid-scale closure method. *Phys. Fluids* **4**, 633-635.

MIKLOSOVIC, D. S., MURRAY, M. M., HOWLE, L. E. & FISH, F. E. 2004. Leading-edge tubercles delay stall on humpback whale (*Megaptera novaeangliae*) flippers. *Phys. Fluids* **16**, L39-L42.

MURATA, S. & NISHIHARA, K. 1976. An experimental study of cross flow fan: 1st report, effects of housing geometry on the fan performance. *Bulletin JSME* **19**, 314-321.

MYERS, R. H., MONTGOMERY, D. C. 1995. *Response surface methodology: process and product optimization using designed experiments.* Wiley.

OUYANG, H., TIAN, J., Li, Y., ZHENG, Z. & DU, Z. 2012. Internal flow and noise investigations about the cross-flow fan with different blade angles. *J. Turb.* **134**, 051023.

PARK, N., LEE, S., LEE, J. & CHOI, H. 2006. A dynamic subgrid-scale eddy viscosity model with a global model coefficient. *Phys. Fluids* **18**, 125109.

PORTER, A. M. & MARKLAND, E. 1970. A study of the cross flow fan. *J. Mech. Eng. Sci.* **12**, 421-431.

TIM, C., LELE, S. K. & MOIN, P. 1993. Boundary conditions for direct computation of aerodynamic sound generation. *AIAA J.* **31**, 1574-1582.

TOFFOLO, A., LAZZARETTO, A. & MARGEGANI, A. D. 2004. An experimental investigation of the flow field pattern within the impeller of a cross-flow fan. *Exp. Therm. Fluid Sci.* **29**,53-64.

TOFFOLO, A., LAZZARETTO, A. & MARTEGANI, A. D. 2004. Cross-flow fan design guidelines for multi-objective performance optimization. *Inst. Mech. Eng., Part A: J. Power Energy* **218**, 33-42.

TUCKEY, P. R. 1983. The aerodynamics and performance of a cross flow fan. Doctoral dissertation, Durham University.

VAN NIEROP, E. A., ALBEN, S. & BRENNER, M. P. 2008. How bumps on whale flippers delay stall: an aerodynamic model. *Phys. Rev. Lett.* **100**, 054502.

YAMAFUJI, K. 1975. Studies on the flow of cross-flow impellers: 2nd report, analytical

study. *Bulletin JSME* **18**, 1425-1431.

직교류 팬 내부 난류 유동의 특성과 혹등고래 혹 구조를 이용한 유동 제어

서울대학교 대학원
기계항공공학부
윤원혁

요약

블레이드 시위 길이와 블레이드 바깥 반경 끝단의 속력을 기준으로 하는 레이놀즈 수가 5,400인 직교류 팬 내부의 유동을 큰 에디 모사와 가상 경계 방법을 이용해 해석하였다. 그 결과, 스테빌라이져 근처의 편심 와류와 유동 유입부를 지나는 블레이드 흡입면에서 발생하는 유동 박리 및 유동 유입부와 리어가이드 사이 모퉁이에서 발생하는 재순환 영역이 관찰되었다. 이와 같은 유동 구조가 팬 성능에 미치는 영향을 알아보기 위해 각 블레이드가 받는 토크 계수의 크기를 방위각 방향으로 측정하였다. 앞서 관찰한 유동장과 토크 계수의 그래프를 비교한 결과, 블레이드 흡입면에서의 유동 박리가 토크 계수의 강한 진동을 유발함을 알 수 있었다. 또한 리어가이드 모퉁이에서 발생한 재순환 영역 역시 주변 블레이드에서 발생하는 유동 박리가 원인임을 알 수 있었고, 근처 블레이드에는 큰 토크가 작용하여 팬의 효율이 저하됨을 알 수 있었다. 이와 같은 분석을 바탕으로 블레이드에서 발생하는 유동 박리를 제어하기 위해 혹등고래 혹 구조를 모사한 생체모방 유동 제어 장치가

사용되었다. 혹 구조를 적용한 결과, 유동 유입부에서 발생하던 유동 박리와 근처 블레이드에 작용하는 토크 계수의 강한 진동이 크게 약화 되었으며, 리어가이드 모퉁이에서 관찰된 재순환 영역과 토크 계수의 봉우리 역시 제거되었다. 또한 매개변수 연구와 응답 표면 방법을 이용하여 최적의 혹 구조 매개변수를 얻을 수 있었으며, 수치해석 결과 팬 효율이 8.45% 향상됨을 관찰하였다.

주요어: 직교류 팬, 유동 박리, 재순환 영역, 토크 계수, 생체모방 유동 제어, 혹등고래 혹 구조

학번: 2016-20660